Impact of the Absorber-Coupling Design for Transition-Edge-Sensor X-Ray Calorimeters

de Wit, M.; Gottardi, L.; Taralli, E.; Nagayoshi, K.; Ridder, M. L.; Akamatsu, H.; Bruijn, M. P.; Hoogeveen, R. W.M.; Gao, J. R.; More Authors

DOI
10.1103/PhysRevApplied.16.044059

Publication date
2021

Document Version
Final published version

Published in
Physical Review Applied

Citation (APA)
de Wit, M., Gottardi, L., Taralli, E., Nagayoshi, K., Ridder, M. L., Akamatsu, H., Bruijn, M. P., Hoogeveen, R. W. M., Gao, J. R., & More Authors (2021). Impact of the Absorber-Coupling Design for Transition-Edge-Sensor X-Ray Calorimeters. *Physical Review Applied*, *16*(4), Article 044059. https://doi.org/10.1103/PhysRevApplied.16.044059

PHYSICAL REVIEW APPLIED **16,** 044059 (2021)

Impact of the Absorber-Coupling Design for Transition-Edge-Sensor X-Ray Calorimeters

M. de Wit,* L. Gottardi, E. Taralli, K. Nagayoshi, M.L. Ridder, H. Akamatsu, M.P. Bruijn,
R.W.M. Hoogeveen, J. van der Kuur, K. Ravensberg, D. Vaccaro, J.-R. Gao,† and J.-W.A. den Herder
NWO-I/SRON Netherlands Institute for Space Research, Niels Bohrweg 4, 2333 CA Leiden, Netherlands

(Received 22 July 2021; revised 10 September 2021; accepted 12 October 2021; published 29 October 2021)

Transition-edge sensors (TESs) are the selected technology for future spaceborne x-ray observatories, such as Athena, Lynx, and HUBS. These missions demand thousands of pixels to be operated simultaneously with high energy-resolving power. To reach these demanding requirements, every aspect of the TES design has to be optimized. Here we present the experimental results of tests on different devices where the coupling between the x-ray absorber and the TES is varied. In particular, we look at the effects of the diameter of the coupling stems and the distance between the stems and the TES bilayer. Based on measurements of the ac complex impedance and noise, we observe a reduction in the excess noise as the spacing between the absorber stem and the bilayer is decreased. We identify the origin of this excess noise to be internal thermal fluctuation noise between the absorber stem and the bilayer. In addition, we see an impact of the coupling on the superconducting transition in the appearance of kinks. Our observations show that these unwanted structures in the transition shape can be avoided with careful design of the coupling geometry. The stem diameter appears to have a significant effect on the smoothness of the TES transition. This observation is still poorly understood, but is of great importance for both ac and dc biased TESs.

DOI: 10.1103/PhysRevApplied.16.044059

I. INTRODUCTION

Transition-edge sensors (TESs) are very sensitive detectors of energy that utilize the sharpness of a superconductor normal-to-superconducting transition [1–3]. TESs are the selected technology in a number of either planned or proposed spaceborne observatories, such as Athena [4], Lynx [5], and HUBS [6]. These missions aim for thousands of pixels to be operated simultaneously with high energy-resolving power. The limited resources available for a satellite-based instrument, such as electrical power, cooling power, and allowable weight, require the use of sophisticated multiplexing schemes, such as time division multiplexing (TDM) [7], frequency division multiplexing (FDM) [8], and others [9–11]. In this paper, we focus on TES-based x-ray microcalorimeters developed for the Athena X-ray Integral Field Unit (X-IFU) instrument [12]. X-IFU will consist of over 3000 multiplexed pixels with a planned spectral resolution of 2.5 eV for 7 keV x-rays.

In order to achieve the demanding requirements set by the X-IFU instrument, every aspect of the TES pixel design has to be optimized. Over the years, much work has been done towards achieving this goal. Research topics included the effect of the thermal conductance on the TES transition width [13–15], the effect of the normal resistance by changing the TES size and aspect ratio [16–18], the noise-mitigating properties of normal-metal features [19–22], and how the energy deposited in the absorbed is transferred to the bilayer [23–26]. In this paper, we expand on this last point by studying how the detailed design of the coupling between the x-ray absorber and the TES bilayer affects the properties of the TES microcalorimeters. The basic layout of the TESs are explained in Sec. II of this paper.

Previous work has shown that the design of the coupling geometry can have a big impact on the detector properties. It was demonstrated that the stems introduce effects of nonequilibrium superconductivity via the proximity effect, affecting the critical temperature and critical current, and influence the small-signal transition parameters $\alpha = (T/R)(\partial R/\partial T)$ and $\beta = (I/R)(\partial R/\partial I)$, and the detector energy resolution and time constants [20,26–28]. Note that these effects were reported for stems with a very large footprint on the bilayer, whereas in this work, we study the effect of much smaller stems, which will allow us to pick up on more subtle differences than those reported previously. We mainly investigate the effect of the diameter of the two stems that connects the absorber to the bilayer, and the spacing between these two. We measured the complex impedance and noise, which are used to estimate the internal thermal conductance in the TES and

---

[*] M.de.Wit@sron.nl

[†] Faculty of Applied Science, Delft University of Technology, Lorentzweg 1, 2628 CJ Delft, The Netherlands

how this is influenced by the geometry. We compare the small-signal limit energy resolution, estimated from the measured noise and transition shape, with the measured noise equivalent power (NEP), and find a good qualitative agreement between the two.

II. DETECTORS AND MEASUREMENT SETUP

We have fabricated an 8 × 8 TES array with four different geometries for the absorber-bilayer coupling. The basic layout of the detectors is shown schematically in Fig. 1(a). The TESs are based on a bilayer made of 35 nm Ti and 200 nm Au, with a sheet resistance of 26 m$\Omega/\Box$. The bilayer is patterned to be an 80×10 μm^2 rectangle with a normal resistance of approximately 200 mΩ. Niobium leads (with critical temperature ~ 9 K) are used to apply a voltage bias to the devices. The bilayers are grown on a 0.5-μm-thick silicon nitride membrane. The TES is connected to a 240×240 μm^2 Au x-ray absorber via two central absorber stems with a height of 3.5 μm, one at each edge of the bilayer. Four additional stems [not shown in Fig. 1(a)] with diameter 5 μm are used to support the absorber on the membrane. The absorber has a thickness of 2.35 μm and a heat capacity of 0.85 pJ/K at 90 mK. Further details about the TESs and the fabrication procedure are given by Nagayoshi *et al.* [29].

To study how the detailed coupling between the absorber and the bilayer affects the detector properties, we vary the geometry of the two absorber stems, as schematically illustrated in Fig. 1(b). We look at the possible effect of the diameter of the two central stems, by comparing two designs with diameters $D = 10$ μm and $D = 5$ μm, both fabricated such that the edge of the bilayer is aligned with the edge of the outer perimeter of the stem. In addition, we look at whether the precise position of the stems is of importance for the final detector performance, by comparing three designs with the same diameter $D = 5$ μm but different spacing between the edge of the bilayer and the edge of the stems, $X = 0, 5$, and 10 μm. The arm connecting the stem and the bilayer is an integral part of the bilayer, deposited in the same step of the fabrication. A schematic close-up view of the connection between the stems and the bilayer is shown in Fig. 1(c). All other properties of the devices are identical to allow for direct comparison.

We characterize the devices using an FDM setup, with which we bias a single pixel at a time within the superconducting transition using an alternating current (ac). The resistance of the TES at a particular bias point is generally specified with respect to the normal resistance R_n. Each of the investigated pixels is connected to a high-Q LC resonator [30] with a bias frequency between 1-5 MHz. An overview of the electrical and thermal circuits is shown in Fig. 2. Further details about the FDM setup are given elsewhere [31]. Most of the results presented in the remainder of this paper do not depend on the bias frequency, and are valid for both ac and direct current (dc) biased pixels. To facilitate straightforward comparison between different readout techniques such as TDM and FDM, we mainly present results from pixels measured at low bias frequencies (< 2 MHz), where frequency-dependent effects unrelated to those discussed in this paper, such as Josephson effects and ac losses, are less significant.

The setup is mounted at the mixing chamber of a cryogen-free dilution refrigerator, and is stabilized at a temperature of 50 mK. External magnetic fields are shielded using a room-temperature μ metal shield and a lead and cryoperm shield at the cold stage. Both the setup and the cryoperm shield are suspended from a Kevlar vibration isolation stage for mechanical decoupling [32]. A more extensive overview of the setup is given elsewhere [18].

For all devices we have determined the critical temperature (T_C) and thermal conductance (G_b) between the TES and the thermal bath. To do so we follow a widely used method in which current-voltage characteristics

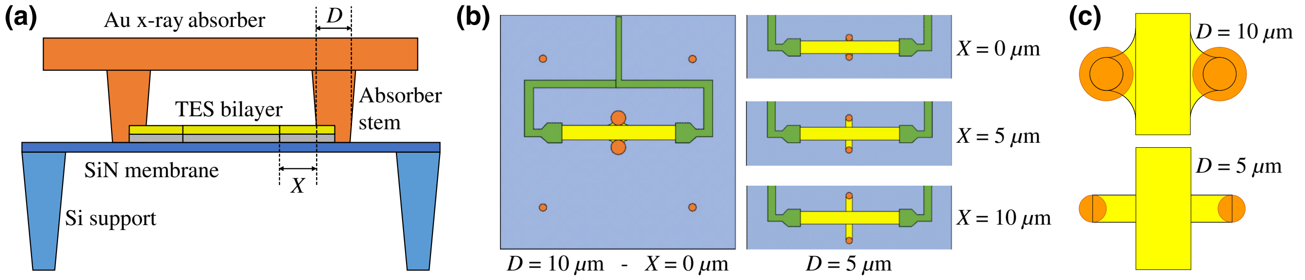

FIG. 1. (a) Schematic of the layout of the TESs. We vary only two aspects of the design: the diameter of the absorber stem D and the spacing between the bilayer and the stem X. (b) Overhead view of the four different designs studied: a single design with $D = 10$ μm and $X = 0$ μm and three designs with $D = 5$ μm and varying spacing, $X = 0, 5$, and 10 μm. The green structures are the niobium leads. (c) Close-up view of the connection between the absorber stems and the bilayer for the $D = 10$ μm (top) and $D = 5$ μm (bottom) designs.

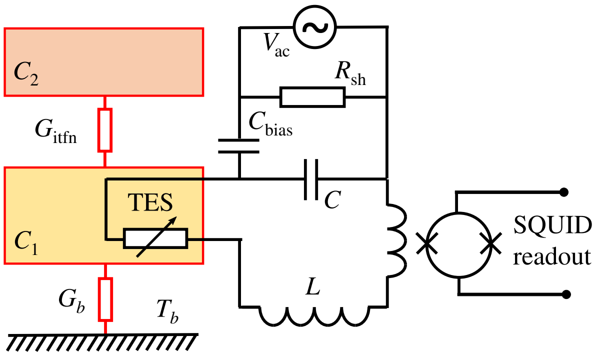

FIG. 2. Schematic of the FDM readout and the two-body thermal model. The TES is coupled to an LC resonator and is readout using a two-stage SQUID. The bias voltage V_{ac} is applied via a shunt resistor R_{sh} and bias capacitor C_{bias}. In the two-body thermal model as used in Sec. III the detector is separated into two bodies, where one body is connected with a thermal conductance G_{itfn} to a second body that is connected to the thermal bath via G_b.

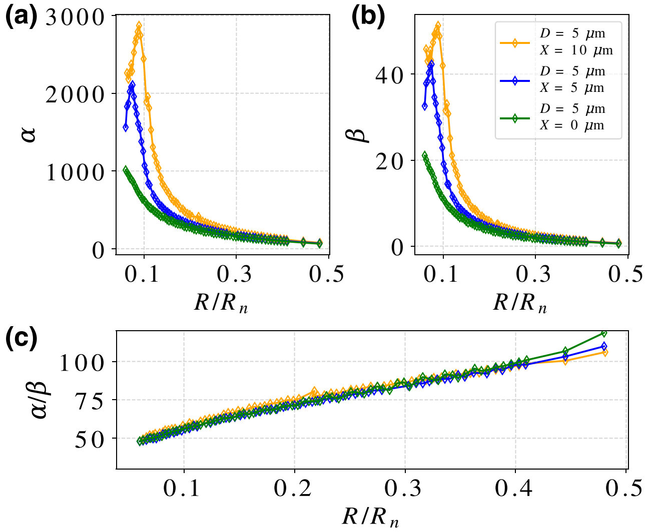

FIG. 3. Results of complex impedance and noise measurements for low-bias-frequency pixels with different stem-bilayer separations: (a) α and (b) β extracted from complex impedance measurements for the relevant part of the normal to superconducting transition; (c) ratio of α/β computed for the same bias points as those shown in (a) and (b).

(I-V curves) are measured at different bath temperatures T_b. These I-V curves are used to determine the amount of Joule heating required to bias the pixel as a function of temperature. This power-temperature ($P(T_b)$) relation is then fitted with the power law $P(T_b) = K\left(T^n - T_b^n\right)$, where K is a geometry-dependent coefficient, T is the TES temperature, and n is an exponent giving information on the nature of the thermal contact. The thermal conductance is then given by $G(T) = nKT^{(n-1)}$. The averaged thermal conductance for all devices is 46.5 pW/K with a standard deviation of 4.6 pW/K at a critical temperature of 81.8 ± 0.2 mK. Given the fact that the thermal conductance of this type of devices is generally proportional to the phonon-emitting perimeter of the TES [13,18,33], the thermal conductance is expected to increase for larger X, with a difference of approximately 7 pW/K between the $X = 0$ and 10 μm devices. This predicted difference has not been resolved in the measured data. The measured critical temperatures for all devices are given in the supplemental material [34].

III. IMPACT OF STEM-BILAYER DISTANCE

We fully characterize the properties of the transition by measuring the complex impedance of the TES [35]. For various points in the transition, a small modulation is added to the bias current with a frequency ranging from 10 Hz–50 kHz, where we record the TES response for each frequency. These data are combined with knowledge of the heat capacity, which is dominated by the x-ray absorber, and thermal conductance to extract the dimensionless derivatives of the resistance with respect to the temperature α and to the current β. We focus on these parameters, as they describe the shape of the superconducting transition and can be used to obtain, among other things, the bandwidth and sensitivity of the detectors. Details of this measurement and analysis under ac bias are given elsewhere [36,37]. Representative data for α and β for low-bias-frequency devices with varying length of the arm between the absorber and the bilayer are shown in Fig. 3.

All the devices show a similar ratio between α/β, visible in Fig. 3(c). However, there are clear differences between the devices low in the resistive transition, as visible in Figs. 3(a) and 3(b). The $X = 5$ μm and $X = 10$ μm devices show high peaks in both α and β, signs of sharp features or kinks in the superconducting transition. No kinks are observed for the $X = 0$ μm devices for all measured bias frequencies. Kinks are regularly observed in devices with normal metal stripes on top of the TES [22,38]. Here we show that also the normal metal of the absorber stems might play a role in the precise location of these kinks in the transition. For the shortest arms with $X = 0$ μm, the kinks are absent or might have shifted to lower resistance values outside of the region of interest. The position of the kink for the $X = 5$ and $X = 10$ μm can shift by a few percent of R_n. When the kinks in the transition are located close to typical bias points of the detectors, they reduce the homogeneity of the array and make achieving a uniform sensitivity and energy gain scale calibration over the full array very challenging. Therefore, the removal of kinks from the transition, in particular the region around

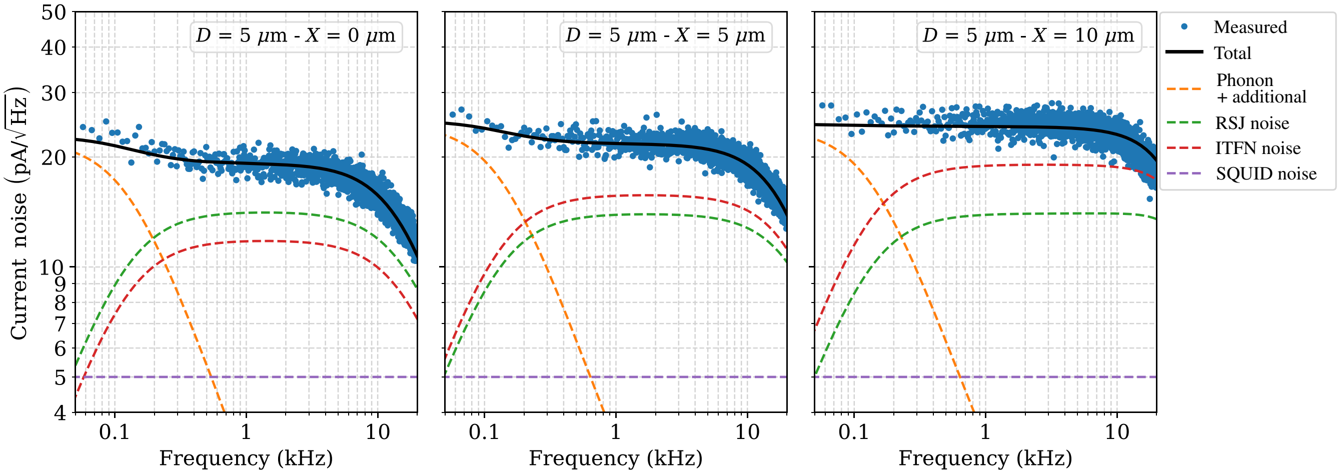

FIG. 4. Example noise spectra measured for the different $D = 0$ μm pixels, measured at $R \sim 0.15$ R_n. Dashed lines represent the calculated noise models: SQUID noise (purple), phonon and additional low-frequency noise (orange), voltage noise from the RSJ model (green), and ITFN (red). The total of all noise sources is given by the solid black line.

0.1–0.2R_n at which devices of this type are typically operated, is of utmost importance. This holds especially for TDM-based systems, where multiple pixels share abreak common bias line and individual tuning of pixels is not possible. In FDM, the removal of kinks is less critical as each pixel can be biased individually at its optimal bias point.

Apart from the complex impedance, for each bias point we have measured the current noise spectrum. Example noise spectra for the three $D = 5$ μm pixels measured at $R = 0.15$ R_n are shown by the blue points in Fig. 4. The roll-off visible at high frequencies results from the bandwidth of the electrical circuit.

We can compare the measured noise spectra with the calculated contributions from various noise sources. First there is the white readout noise of the SQUID at approximately 5 pA/$\sqrt{\text{Hz}}$. The second noise contribution is the phonon noise originating from thermal fluctuations between the TES and the heat bath, with a power spectral density given by $S_{P,\text{ph}} = 2k_BT^2G_b\left((T_b/T)^{n+2} + 1\right)$. Above approximately 200Hz the phonon noise has a roll-off determined by the thermal bandwidth of the detector. Additional low-frequency noise sources, such as vibrations and stray photons, are summed under the name *additional low-frequency noise*. This low-frequency additional noise is not considered fundamental for the TES as it can be mitigated with a proper design of the setup. For the results presented in this paper, the most interesting is the noise at higher frequencies within the electrical bandwidth of the detector, typically characterized around 1 kHz. At these frequencies the principal source of noise is Johnson noise from the TES resistance. At low frequencies the Johnson noise is suppressed by the electrothermal feedback [39], whereas at high frequencies the roll-off results from the bandwidth of the readout. It has recently been shown that for this type of devices the Johnson noise is best described by the resistively shunted junction (RSJ) model [37,40,41], given by

$$S_{V,\text{RSJ}} = 4k_B\text{TR}\left(1 + \frac{5}{2}\beta + \frac{3}{2}\beta^2\right), \qquad (1)$$

with k_B being the Boltzmann constant. All of these main sources of noise are shown as the various dashed lines in Fig. 4. The details on how these contributions are calculated have recently been covered extensively by Gottardi *et al.* [37]. From Fig. 4 it is immediately apparent that the sum of these noise sources is insufficient to fully explain the measured noise. Therefore, we express the factor of difference between the measured noise and the predicted noise at frequency 1 kHz using the parameter M^2, defined by

$$M^2 = \left(S_{V,\text{data}} - S_{V,\text{RSJ}}\right)/S_{V,\text{data}}. \qquad (2)$$

Figure 5(a) shows M^2 for various bias points in the transition for the different designs, showing a clear rise in M^2 as X increases.

To explain the additional noise in the kilohertz range, we interpret it as resulting from internal thermal fluctuation noise (ITFN) within the detector itself [37,42]. ITFN occurs when there are distributed heat capacities inside the detector connected by internal thermal impedances. We apply a two-body model, in which the detector is separated into two bodies, where one body is connected with a thermal conductance G_{itfn} to a second body that is connected to the thermal bath via G_b. A schematic of this two-body model is shown in Fig. 2. Details about the implementation of this model for our detectors are given by Gottardi

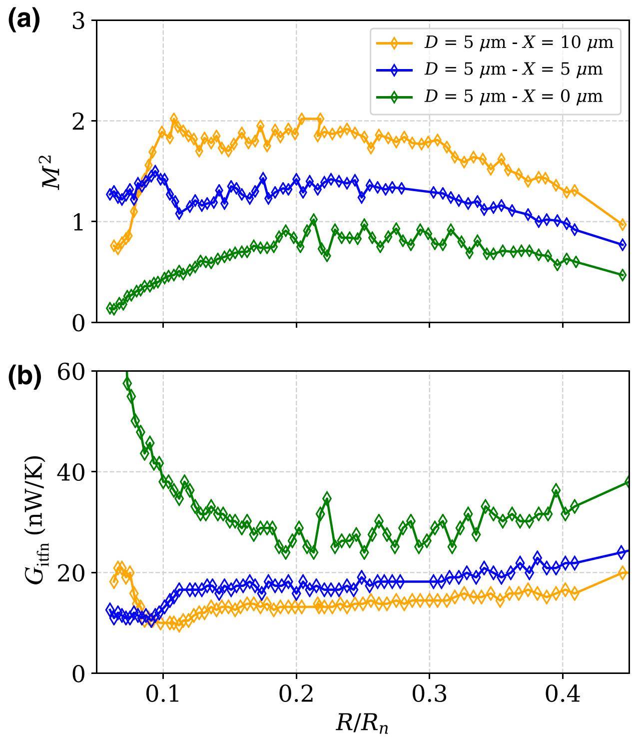

FIG. 5. (a) Excess noise factor defined with respect to expected noise in the RSJ model $S_{V,\mathrm{RSJ}}$ for the same bias points shown in Fig. 3 and (b) G_{itfn} required to minimize the excess noise factor for each bias point.

et al. [37]. Thermal excitations in one of these bodies lead to thermal fluctuation noise, analogous to the previously mentioned phonon noise, with a power spectral density given by $S_{P,\mathrm{itfn}} = 4k_BT^2G_{\mathrm{itfn}}$ [43,44]. This contribution is shown as the red dashed lines in Fig. 4. Note that the shape of the ITFN is similar to the RSJ Johnson noise due to the conversion of power to current noise via the power-to-current responsivity and the TES circuit inductance. Here G_{itfn} is treated as a free parameter to be varied such that M^2 is minimized. The resulting G_{itfn} is shown in Fig. 5(b). As expected, the internal thermal conductance decreases as X increases. At $R/R_n \sim 20\%$, the extracted G_{itfn} increases from approximately 14 nW/K for $X = 10$ μm to around 18 nW/K for $X = 5$ μm, and, finally, to about 27 nW/K for $X = 0$ μm.

The internal thermal conductance is believed to be a combination of the internal thermal conductance of the bilayer G_{bl}, and the limited thermal conductance of the arm between the absorber stem and the bilayer, G_{arm}. Using the simplest possible thermal model in which the different thermal components are connected in series, G_{arm} can be estimated from the measured G_{itfn} using

$$G_{\mathrm{arm}} = \left(\frac{1}{G_{\mathrm{itfn}}} - \frac{1}{G_{\mathrm{bl}}}\right)^{-1}. \tag{3}$$

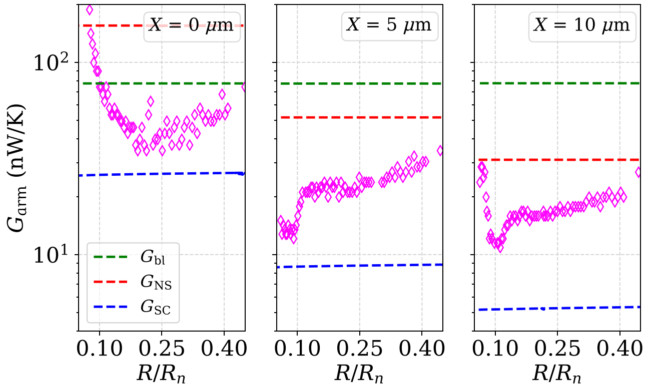

FIG. 6. Estimated value of G_{arm}, assuming a constant bilayer thermal conductance given by the Wiedemann-Franz law (green dashed line). The blue dashed line shows the arm thermal conductance when it remains superconducting (ignoring the temperature dependence of the gap). The red dashed line shows the arm thermal conductance when it is in the normal state (and, thus, follows the Wiedemann-Franz law). We take the effective length of the arm equal to $X + D/2$.

The internal thermal conductance of the bilayer is estimated by using the Wiedemann-Franz law, $G_{\mathrm{bl}} = L_0T/R_\square$, with $L_0 = 2.45 \times 10^{-8}\Omega$ WK^{-2} and $R_\square$ the sheet resistance of the bilayer [37]. For the 80×10 μm^2 devices, $G_{\mathrm{bl}} = 77$ nW/K. The estimated G_{arm} is shown as the magenta points in Fig. 6.

To understand the origin of the limited thermal conductance of the arm, we estimate it in two limiting regimes. The upper limit is given by the normal state thermal conductance of the arm G_{NS}, which again is estimated using the Wiedemann-Franz law. In this case the resistance of the arm is calculated using an effective length $X + D/2$, the full length of the arm including the end part covered by the absorber stem. This upper limit is shown in Fig. 6 as the red dashed lines. The lower limit is obtained by assuming that the arm remains superconducting. As Cooper pairs cannot transport heat the thermal conductance is purely governed by the fraction of depaired electrons, which is dictated by the temperature dependent superconducting gap $\Delta(T)$ and the thermal excitation energy k_BT. Thus, the thermal conductance can be estimated using

$$G_{\mathrm{SC}} = G_{\mathrm{NS}}\,\exp\left(-\frac{\Delta(T)}{k_BT}\right). \tag{4}$$

Knowledge about the temperature dependence of the superconducting gap is required to evaluate this equation. For a conventional s-wave superconductor at $T \approx T_C$, this dependence is given by

$$\Delta(T) \approx 1.74\Delta(0)\sqrt{1 - \frac{T}{T_C}}, \tag{5}$$

with $\Delta(0) = 1.764\ k_B T_C$ the gap at $T = 0$ [45]. However, this is not valid in the presence of the proximity effect, which significantly alters the size of the gap close to the T_C of the bilayer. Therefore, we simplify the problem and derive a lower limit for the thermal conductance by neglecting the temperature dependence of the gap and using $\Delta(T) = \Delta(0)$. The resulting G_{SC} is shown as the blue dashed lines in Fig. 6. Indeed the values for G_{arm} extracted from the experimental data fall between these two boundaries, supporting the interpretation that the arm partially remains superconducting with a $\Delta(T)$ that is suppressed compared with the ideal $T = 0$ value, but remains finite.

The previous analysis clearly indicates that a small but significant reduction of the excess noise can be achieved by keeping the stem as close to the bilayer as possible, or perhaps by even placing the stems on top of the bilayer [46]. Note that after reducing the ITFN, the performance of this type of device under these conditions will remain limited by the noise resulting from the weak-link effect as described by the RSJ model.

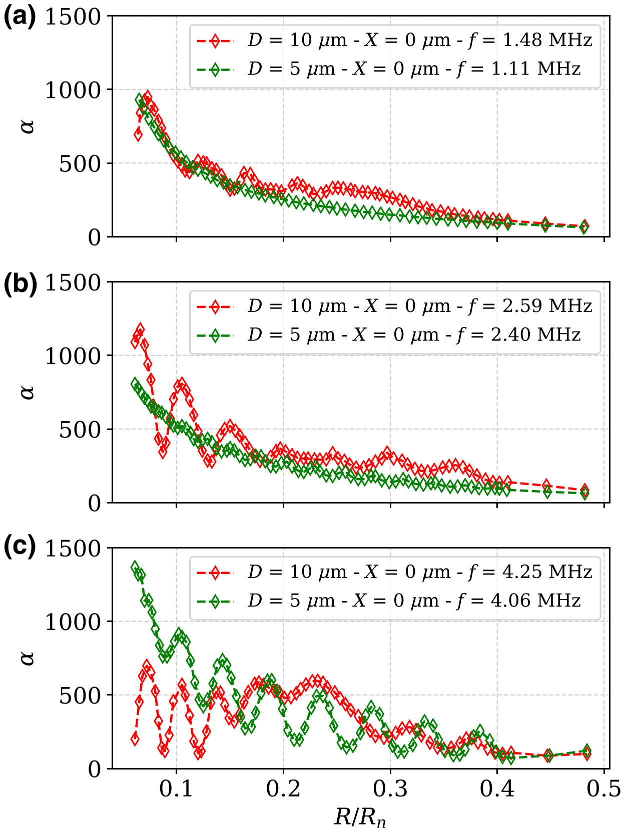

FIG. 7. Measured α versus R/R_n for pixels with different stem diameters. We show three sets of pixels at different bias frequencies: (a) 1.1–1.5 MHz, (b) 2.4–2.6 MHz, and (c) 4.1–4.3 MHz.

IV. IMPACT OF STEM-BILAYER DIAMETER

The main effects of the stem diameter are visible in the measured α, shown in Fig. 7, and excess noise, shown in Fig. 8. In these figures, we focus on the designs with $X = 0\ \mu$m. Three different sets of pixels are selected, measured at (a) low, (b) mid, and (c) high bias frequencies, the precise values of which are indicated in the legend of Fig. 7.

Changing the stem diameter from $D = 10$ to $D = 5\ \mu$m does not change the overall trend of α. However, there is a striking difference between how α, and consequently β and M^2, change throughout the transition. The $D = 10\ \mu$m devices show large oscillations of α for different bias points. These oscillations are typically attributed to the weak-link effect in these detectors resulting from the interaction between the high T_C Nb leads and the low T_C bilayer. This weak-link effect scales with the superconducting phase difference $\phi \propto \sqrt{PR}/\omega$ (with P the detector power and ω the bias frequency), and with the length of the link and the difference in critical temperature of the coupled superconductors [47]. However, the amplitude of the oscillations is much smaller for all $D = 5\ \mu$m devices, except for those measured at the highest bias frequencies as visible in Fig. 7(c). To understand the underlying mechanism for why the smaller stem diameter improves the smoothness of the superconducting transition, more devices with different stem diameters should be studied. However, we speculate about one possible explanation in Sec. VI.

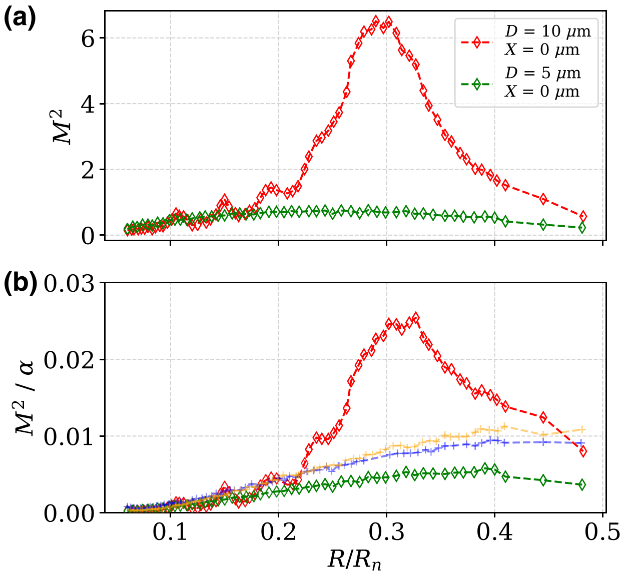

FIG. 8. (a) Excess noise M^2 and (b) M^2 / α for low-frequency pixels with different stem diameters. In (a), data are shown for the $X = 0, D = 10\ \mu$m (red) and $X = 0, D = 5\ \mu$m (green) devices. In (b), also the data for the $X = 5\ \mu$m (blue) and $X = 10\ \mu$m (yellow) devices are shown as a reference.

Another interesting feature of the smaller stem diameter is visible in the excess noise in Fig. 8(a). For all of the five devices studied in this work with $D = 10\ \mu$m, a peak in the excess noise is visible between $R = 0.2R_n$ and $0.5R_n$. This peak is never observed for any of the devices with $D = 5\ \mu$m. We present this bump in terms of the excess noise parameter instead of using ITFN, as we expect the ITFN to be very small for the $X = 0\ \mu$m devices. Therefore, we do not expect that it is justified to explain this particular feature of the noise using ITFN. The $D = 5\ \mu$m devices do show a bump in the transition around $R \approx 0.1R_n$, visible in Fig. 3, but in those cases the increase in α is correlated with an increase in M^2. This is not the case for the $D = 10\ \mu$m devices, a fact that becomes clear when looking at Fig. 8(b), in which we plot M^2/α. The stark difference in the ratio of M^2 and α between the $D = 10\ \mu$m data (red points) and the other data signifies the difference in nature of the bump in the excess noise.

V. NEP AND ENERGY RESOLUTION

Arguably the most important figure of merit for a microcalorimeter is the energy resolution, i.e., the capability to resolve different photon energies. In this section, we demonstrate the effect of the absorber-coupling geometry in two ways. First, we evaluate the energy resolution estimated from the integrated NEP at 5.9 keV for bias points between $R = 0.05R_n$ and $0.30R_n$. The $\mathrm{NEP}(f)^2 = \langle|N(f)|^2\rangle / |S(f)|^2$ is the ratio between the average noise power spectral density and the squared detector responsivity. The theoretically achievable energy resolution is then given by

$$\Delta E_{\mathrm{NEP}} = 2.355 \left(\int_0^\infty \frac{4}{\mathrm{NEP}(f)^2}\, df \right)^{-\frac{1}{2}}. \qquad (6)$$

The prediction from the integrated NEP does not account for nonlinearity in the detector in the large-signal limit, but for the devices reported here we have empirically found that it is generally still a good predictor for the achievable energy resolution. In addition, we can use α, β, and M^2, as shown in Secs. III and IV, to calculate the expected energy resolution in the small-signal and strong electro-thermal feedback (ETF) limit for each bias point, using

$$\Delta E_{\mathrm{THE}} = 2\sqrt{2\ln 2}\sqrt{4k_B T^2 \frac{C}{\alpha}\sqrt{\left(1 + \frac{5}{2}\beta + \frac{3}{2}\beta^2\right)(1 + M^2)}}. \qquad (7)$$

This equation considers all excess noise to be of similar nature to the Johnson noise, and does not take into account the full two-body responsivity. However, for the high ratio between G_{itfn} and G_b reported here the effect of this simplification is expected to be small. The results for the NEP and expected energy resolution are shown in Fig. 9 for four different pixels, one of each design, measured at low bias frequencies. In absolute terms, a relatively large difference is observed between the NEP and estimated ΔE. This is most likely the result of the fact that our detectors are working outside of the small-signal limit for 5.9 keV x-rays. Note that the increase in NEP and ΔE seen in the $D = 10\ \mu$m, $X = 0\ \mu$m device at higher R/R_n is caused by the bump in the excess noise shown in Fig. 8.

The NEP and calculated ΔE qualitatively give the same results, and confirm the trends identified previously. The best energy resolutions are expected for the devices with $X = 0\ \mu$m. As the length of the arm between the absorber and the bilayer increases, the energy resolution becomes worse. This observation holds over the full bias frequency range. The increase in the energy resolution is about 0.2–0.4 eV, and clearly indicates that maximizing the thermal conductance between the absorber and the bilayer is of great importance to optimize the resolution. The effect of the stem diameter is much less pronounced, with only a very small reduction of less than 0.1 eV for both the NEP and ΔE. This is not completely unexpected. If we assume that the gold in the absorber stem has a electrical resistivity $\rho_{Au} = 1$ nΩ m, similar to previously reported values [42], the Wiedemann-Franz law can be used to estimate a thermal conductance of the stem (with height 3.5 μm). This leads to $G_{\mathrm{stem}} = 11\ \mu$W/K and 45 μW/K for the 5 μm and 10 μm diameter stems, respectively. For both diameters, G_{stem} is much higher that the estimated thermal

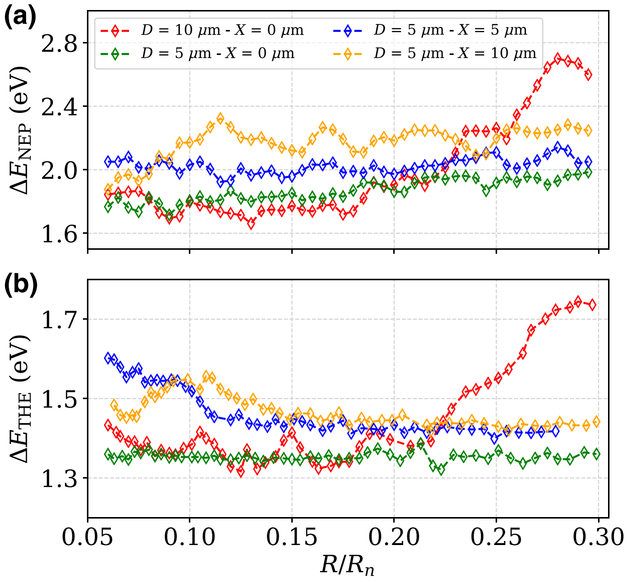

FIG. 9. (a) Measured NEP and (b) small-signal limit energy resolution calculated using Eq. (7). The NEP is measured at the optimal bias frequency for each value of R/R_n.

conductance of the arm, and therefore does not play a significant role in the noise.

VI. DISCUSSION

In the previous two sections, we have shown a number of effects of the absorber coupling that are as of yet poorly understood: (1) the appearance of kinks in the transition for different values of X; (2) increased oscillations in the transition for the $D = 10$ μm devices compared with the $D = 5$ μm devices; (3) the presence of unexplained bump in the excess noise for the $D = 10$ μm devices. Although these three observed effects appear separated at first glance, we believe that they all have the same underlying cause, which is the distribution of the current within the central part of the bilayer and the absorber stems.

As stated in Sec. III, kinks in the transition have been linked to the presence of noise-mitigating normal metal structures on top of the TES, as was done for instance by Wakeham *et al.* [22]. In that work, the authors associate the kinks in $R(T)$ and α with regions of large change in the $I(B)$ curve. This correlation is interpreted as resulting from changes in the supercurrent distribution within the TES. Although for our devices we see no significant discontinuities in the $I_C(B)$ curve such as those reported by Wakeham *et al.* (see the supplemental information for representative $I_C(B)$ curves for each design [34]), finite-element analysis of our devices indicates that, in fact, the current distribution should be expected to be different between the designs.

To understand these differences, we have to consider the details of the geometric coupling between the stems and the bilayer, as shown in Figs. 1(b) and 1(c). For the $D = 10$ μm devices, the arm connected to the stem is broad, and it is connected to the bilayer with a rounded corner. As a result of this, the current at the center of the bilayer between the stems can split, with one part flowing in the bilayer, and another part flowing through the arms and stems. The precise distribution of the current depends on the ratio between the resistance of the bilayer, which changes with the bias point, and the (interface) resistance of the stems. However, for the $D = 5$ μm devices the current density in the arms drops severely within a few micrometers from the edge of the bilayer, owing to current crowding resulting from the combination of the small width of the arms and the sharp corners between the arms and the bilayer. The reason why the differences in the current distribution are not observed in the $I_C(B)$ curves are not fully understood. The simplest explanation might be that the impact was too small to be resolved in our measurements, as the differences in current distribution are confined to a very small fraction of the bilayer close to the stems.

This returns us to our observation of the kinks in α and β for the devices of varying X. The geometric suppression of the current distribution in the arms leads to a distinction between the $X = 0$ μm devices, for which current can just flow underneath or through the normal metal of the stem, and the devices with $X > 0$, where this is not the case. Although the exact origin for the appearance of the kinks remains elusive, this would explain why we see such a stark difference between the $X = 0$ devices where no kinks are seen above $R = 0.05R_n$ and the $X > 0$ devices where we have always observed a kink without a clear correlation between the kink position and the length of the arm.

Now let us consider the excess noise bump for the $D = 10$ μm devices. As explained previously, in these devices a part of the current can easily flow through the stem, where the precise distribution of the current depends on the bias point and the resistance of the stem. Following the same procedure as outlined in Sec. III, for the $D = 10$ μm device we extract an estimated thermal conductance of the arm of approximately 60 nW/K, corresponding to a resistance of approximately 30 mΩ, possibly located at the interface between the arm and the stem. This resistance is comparable to the square resistance of the bilayer. Thus, the distribution of the current at the center of the TES can change significantly within the resistive transition. Although it is not possible to draw hard conclusions based on only a single device design, we speculate that the increased excess noise is related to current flowing through the stems. This would explain the disappearance of excess noise low in the transition where the bilayer resistance becomes far less than the estimated resistance of the arm, and most of the current stays within the bilayer.

The final topic is the reduction in the oscillations in the transition parameters for the $D = 5$ μm, $X = 0$ μm devices compared with the $D = 10$ μm devices, as reported in Sec. IV. Typically these oscillations are explained as coming from the weak-link effect resulting from a simple SS′S junction consisting of the niobium leads (S) coupled to the Ti/Au bilayer (S′). This explanation is probably correct for the small stem diameter devices, where the supercurrent is restricted to flow purely in the bilayer, and almost no current actually crosses the stems, as discussed previously. This simple weak-link effect is characterized by oscillations with a constant period (when plotted as a function of the TES voltage) and gradually changing amplitude, precisely what is observed for the green curves in Fig. 7. However, for the large-diameter devices the situation is different. In this case, simulations suggest that in particular for bias points high in the resistive transition, a significant part of the current does not flow through the center of the bilayer, but instead is diverted along the stems. For this situation, we hypothesize that the TES has to be modeled as two junctions in parallel, the first being the previously introduced SS′S junction, and the second being made up of two S′NS′ junctions between the bilayer and the normal metal stems (N). This introduces a combined weak-link effect with two different characteristic oscillation periods. Signatures of the mixing of these periods are visible in the red data of Fig. 7, in particular for the higher-frequency pixel shown in Fig. 7(c). In addition, in this model, the impact of the S′NS′ junctions should be less in the transition, where the bilayer resistance starts to drop below the resistance of the stems, meaning a larger part of the current is confined to the central part of the bilayer. Thus, for low resistance values, the oscillations should become cleaner with a similar period to that observed in the $D = 5\ \mu$m devices, another feature that is clearly visible in Fig. 7(c) for $R < 0.15R_n$. The transition between the single-junction and double-junction behavior overlaps with the low-resistance flank of the measured excess noise bumps.

In order to test the idea that all these effects indeed originate from a splitting of the supercurrent between the bilayer and the absorber stems, we are currently fabricating a number of new devices. For example, one of the new devices will contain two 5 μm diameter stems which are not connected via arms to the bilayer, but are instead placed directly on top of the bilayer. This design will considerably constrict the current flow in the central part of the bilayer, forcing a larger portion of the current to travel underneath the stems. This design should act like the exaggerated version of the current $D = 10\ \mu$m device, and, if our current hypothesis of the double junction is correct, should exhibit a significantly larger mixed weak-link effect than what is measured in the current $D = 5\ \mu$m devices.

VII. CONCLUSIONS

We have studied the effect of the detailed geometry for the thermal coupling between the x-ray absorber and the bilayer, with a particular focus on the diameter of the two stems that connect the absorber to the TES bilayer, and the spacing between the stems and the bilayer.

Based on measurements of the noise, we have found that the noise is reduced for shorter arms, an observation that we explain in terms of a higher internal thermal conductance between the absorber and the TES. In addition, we observe that the position of kinks in the superconducting transition is affected by the spacing between the stems. Comparing the devices with different stem diameters resulted in the striking observation that the smoothness of the transition seems to be improved significantly for the smaller stem diameter. Although a more thorough investigation is required to fully understand the responsible mechanism, we hypothesize that the observed effects are related to variations in the current distribution within the bilayer and the stems. Additional devices of different geometries, such as that we discuss at the end of Sec. VI, should help to definitively confirm these ideas. The new devices are currently under fabrication.

The conclusion of this study is that the stems should be placed as close to the bilayer as possible in order to reduce the ITFN, leading to an improved energy resolution of up to 0.4 eV. This observation is consistent with the results from similar studies [46]. To maximize the thermal conductance between the absorber and the bilayer, often the choice is made to connect the stems to normal metal edge banks running along the length of the TES [21,22]. Unfortunately, the banks lower the resistance of the devices, making them incompatible with ac biased readout systems such as FDM in which high resistance devices perform best. In any case, the presented results indicate that ITFN can be mitigated to a sufficiently low level by a careful design of the coupling structure. The optimization of the stem diameter is more complicated. For the energy resolution, increasing the diameter could further reduce the ITFN and give better energy resolutions at certain bias points (even though the effect will be quite modest). However, our results suggest that reducing the stem diameter, or perhaps only using a single supporting stem or making a sharper edge for the connection between the stem and the bilayer, might greatly improve the smoothness and uniformity of the normal-to-superconducting transition, a feature that is of great importance for the successful operation of a large number of TESs in any multiplexing scheme.

ACKNOWLEDGMENTS

SRON is supported financially by NWO, the Netherlands Organization for Scientific Research. This work is partly funded by European Space Agency (ESA) and coordinated with other European efforts under ESA CTP contract ITT AO/1-7947/14/NL/BW.

DATA AVAILABILITY

The data that support the findings of this study are available from the corresponding author upon reasonable request.

[1] K. D. Irwin and G. C. Hilton, Transition-edge sensors, Top. Appl. Phys. **99**, 63 (2005).

[2] J. N. Ullom and D. A. Bennett, Review of superconducting transition-edge sensors for x-ray and gamma-ray spectroscopy, Supercond. Sci. Technol. **28**, 084003 (2015).

[3] L. Gottardi and K. Nagayashi, A review of X-ray microcalorimeters based on superconducting transition edge sensors for astrophysics and particle physics, Appl. Sci. (Switzerland) **11**, 3793 (2021).

[4] D. Barret, A. Decourchelle, A. Fabian, M. Guainazzi, K. Nandra, R. Smith, and J. W. den Herder, The athena space X-ray observatory and the astrophysics of hot plasma†, Astronomische Nachrichten **341**, 224 (2020).

[5] J. A. Gaskin and D. A. Swartz, Lynx X-ray observatory: An overview, J. Astron. Telescopes, Instrum., Syst. **5**, 1 (2019).

[6] W. Cui, L. B. Chen, B. Gao, F. L. Guo, H. Jin, G. L. Wang, L. Wang, J. J. Wang, W. Wang, Z. S. Wang, Z. Wang,

F. Yuan, and W. Zhang, HUBS: Hot universe baryon surveyor, J. Low. Temp. Phys. **199**, 502 (2020).

[7] M. Durkin, *et al.*, Demonstration of athena X-IFU compatible 40-row time-division-multiplexed readout, IEEE Trans. Appl. Supercond. **29**, 1 (2019).

[8] H. Akamatsu, L. Gottardi, J. van der Kuur, C. P. de Vries, M. P. Bruijn, J. A. Chervenak, M. Kiviranta, A. J. van den Linden, B. D. Jackson, A. R. Miniussi, K. Ravensberg, K. Sakai, S. J. Smith, and N. Wakeham, Progress in the development of frequency-domain multiplexing for the X-ray integral field unit on board the athena mission, J. Low. Temp. Phys. **199**, 737 (2020).

[9] K. M. Morgan, B. K. Alpert, D. A. Bennett, E. V. Denison, W. B. Doriese, J. W. Fowler, J. D. Gard, G. C. Hilton, K. D. Irwin, Y. I. Joe, G. C. O'Neil, C. D. Reintsema, D. R. Schmidt, J. N. Ullom, and D. S. Swetz, Code-division-multiplexed readout of large arrays of TES microcalorimeters, Appl. Phys. Lett. **109**, 112604 (2016).

[10] D. A. Bennett, J. A. B. Mates, S. R. Bandler, D. T. Becker, J. W. Fowler, J. D. Gard, G. C. Hilton, K. D. Irwin, K. M. Morgan, C. D. Reintsema, K. Sakai, D. R. Schmidt, S. J. Smith, D. S. Swetz, J. N. Ullom, L. R. Vale, and A. L. Wessels, Microwave SQUID multiplexing for the Lynx x-ray microcalorimeter, J. Astron. Telescopes, Instrum., Syst. **5**, 1 (2019).

[11] Y. Nakashima, F. Hirayama, S. Kohjiro, H. Yamamori, S. Nagasawa, A. Sato, S. Yamada, R. Hayakawa, N. Y. Yamasaki, K. Mitsuda, K. Nagayoshi, H. Akamatsu, L. Gottardi, E. Taralli, M. P. Bruijn, M. L. Ridder, J. R. Gao, and J. W. Den Herder, Low-noise microwave SQUID multiplexed readout of 38 x-ray transition-edge sensor microcalorimeters, Appl. Phys. Lett. **117**, 3 (2020).

[12] F. Pajot, *et al.*, The athena X-ray integral field unit (X-IFU), J. Low. Temp. Phys. **193**, 901 (2018).

[13] J. P. Hays-Wehle, D. R. Schmidt, J. N. Ullom, and D. S. Swetz, Thermal conductance engineering for high-speed TES microcalorimeters, J. Low. Temp. Phys. **184**, 492 (2016).

[14] K. M. Morgan, C. G. Pappas, D. A. Bennett, J. D. Gard, J. P. Hays-Wehle, G. C. Hilton, C. D. Reintsema, D. R. Schmidt, J. N. Ullom, and D. S. Swetz, Dependence of transition width on current and critical current in transition-edge sensors, Appl. Phys. Lett. **110**, 2 (2017).

[15] X. Zhang, S. M. Duff, G. C. Hilton, P. J. Lowell, K. M. Morgan, D. R. Schmidt, and J. N. Ullom, Controlling the thermal conductance of silicon nitride membranes at 100 mK temperatures with patterned metal features, Appl. Phys. Lett. **115**, 052601 (2019).

[16] K. Sakai, *et al.*, Study of dissipative losses in AC-biased Mo/Au bilayer transition-edge sensors, J. Low. Temp. Phys. **193**, 356 (2018).

[17] K. M. Morgan, D. T. Becker, D. A. Bennett, W. B. Doriese, J. D. Gard, K. D. Irwin, S. J. Lee, D. Li, J. A. Mates, C. G. Pappas, D. R. Schmidt, C. J. Titus, D. D. Van Winkle, J. N. Ullom, A. Wessels, and D. S. Swetz, Use of transition models to design high performance TESs for the LCLS-II soft X-ray spectrometer, IEEE Trans. Appl. Supercond. **29**, 1 (2019).

[18] M. De Wit, L. Gottardi, E. Taralli, K. Nagayoshi, M. L. Ridder, H. Akamatsu, M. P. Bruijn, M. D'Andrea, J. Van Der Kuur, K. Ravensberg, D. Vaccaro, S. Visser, J. R. Gao, and J. W. Den Herder, High aspect ratio transition edge sensors for x-ray spectrometry, J. Appl. Phys. **128**, 224501 (2020).

[19] J. N. Ullom, W. B. Doriese, G. C. Hilton, J. A. Beall, S. Deiker, W. D. Duncan, L. Ferreira, K. D. Irwin, C. D. Reintsema, and L. R. Vale, Characterization and reduction of unexplained noise in superconducting transition-edge sensors, Appl. Phys. Lett. **84**, 4206 (2004).

[20] J. E. Sadleir, S. J. Smith, I. K. Robinson, F. M. Finkbeiner, J. A. Chervenak, S. R. Bandler, M. E. Eckart, and C. A. Kilbourne, Proximity effects and nonequilibrium superconductivity in transition-edge sensors, Phys. Rev. B - Condens. Matter and Mater. Phys. **84**, 184502 (2011).

[21] A. R. Miniussi, J. S. Adams, S. R. Bandler, J. A. Chervenak, A. M. Datesman, M. E. Eckart, A. J. Ewin, F. M. Finkbeiner, R. L. Kelley, C. A. Kilbourne, F. S. Porter, J. E. Sadleir, K. Sakai, S. J. Smith, N. A. Wakeham, E. J. Wassell, and W. Yoon, Performance of an X-ray microcalorimeter with a 240 μm absorber and a 50 μm TES bilayer, J. Low. Temp. Phys. **193**, 337 (2018).

[22] N. A. Wakeham, J. S. Adams, S. R. Bandler, J. A. Chervenak, A. M. Datesman, M. E. Eckart, F. M. Finkbeiner, R. L. Kelley, C. A. Kilbourne, A. R. Miniussi, F. S. Porter, J. E. Sadleir, K. Sakai, S. J. Smith, E. J. Wassell, and W. Yoon, Effects of normal metal features on superconducting transition-edge sensors, J. Low. Temp. Phys. **193**, 231 (2018).

[23] C. A. Kilbourne, S. R. Bandler, A. D. Brown, J. A. Chervenak, E. Figueroa-Feliciano, F. M. Finkbeiner, N. Iyomoto, R. L. Kelley, F. S. Porter, and S. J. Smith, Uniform high spectral resolution demonstrated in arrays of TES x-ray microcalorimeters, UV, X-Ray, and Gamma-Ray Space Instrum. Astron. XV **6686**, 668606 (2007).

[24] Y. Takei, L. Gottardi, H. F. C. Hoevers, P. A. J. de Korte, J. van der Kuur, M. L. Ridder, and M. P. Bruijn, Characterization of a high-performance Ti/Au TES microcalorimeter with a central Cu absorber, J. Low. Temp. Phys. **151**, 161 (2008).

[25] S. J. Smith, J. S. Adams, M. E. Eckart, C. N. Bailey, S. R. Bandler, J. A. Chervenak, F. M. Finkbeiner, R. L. Kelley, C. A. Kilbourne, F. S. Porter, and J. E. Sadleir, Small pitch transition-edge sensors with broadband high spectral resolution for solar physics, J. Low. Temp. Phys. **167**, 168 (2012).

[26] S. J. Smith, J. S. Adams, S. R. Bandler, S. E. Busch, J. A. Chervenak, M. E. Eckart, F. M. Finkbeiner, R. L. Kelley, C. A. Kilbourne, S. J. Lee, J. P. Porst, F. S. Porter, and J. E. Sadleir, Characterization of Mo/Au transition-edge sensors with different geometric configurations, J. Low. Temp. Phys. **176**, 356 (2014).

[27] S. R. Bandler, R. P. Brekosky, A. D. Brown, J. A. Chervenak, E. Figueroa-Feliciano, F. M. Finkbeiner, N. Iyomoto, R. L. Kelley, C. A. Kilbourne, F. S. Porter, J. Sadleir, and S. J. Smith, Performance of TES X-ray microcalorimeters with a novel absorber design, J. Low. Temp. Phys. **151**, 400 (2008).

[28] S. J. Smith, J. S. Adams, C. N. Bailey, S. R. Bandler, S. E. Busch, J. A. Chervenak, M. E. Eckart, F. M. Finkbeiner, C. A. Kilbourne, R. L. Kelley, S. J. Lee, J. P. Porst, F. S. Porter, and J. E. Sadleir, Implications of weak-link behavior on

the performance of Mo/Au bilayer transition-edge sensors, J. Appl. Phys. **114**, 074513 (2013).

[29] K. Nagayoshi, M. L. Ridder, M. P. Bruijn, L. Gottardi, E. Taralli, P. Khosropanah, H. Akamatsu, S. Visser, and J. R. Gao, Development of a Ti/Au TES microcalorimeter array as a backup sensor for the athena/X-IFU instrument, J. Low. Temp. Phys. **199**, 943 (2020).

[30] M. P. Bruijn, L. Gottardi, R. H. Den Hartog, H. F. Hoevers, M. Kiviranta, P. A. De Korte, and J. Van Der Kuur, High-Q LC filters for FDM read out of cryogenic sensor arrays, J. Low. Temp. Phys. **167**, 695 (2012).

[31] H. Akamatsu, L. Gottardi, J. van der Kuur, C. P. de Vries, K. Ravensberg, J. S. Adams, S. R. Bandler, M. P. Bruijn, J. A. Chervenak, C. A. Kilbourne, M. Kiviranta, A. J. van der Linden, B. D. Jackson, and S. J. Smith, Development of frequency domain multiplexing for the X-ray integral field unit (X-IFU) on the athena, Space Telescopes and Instrum. 2016: Ultraviolet to Gamma Ray **9905**, 99055S (2016).

[32] L. Gottardi, H. J. van Weers, J. Dercksen, H. Akamatsu, M. P. Bruijn, J. R. Gao, B. D. Jackson, P. Khosropanah, J. van der Kuur, K. Ravensberg, and M. Ridder, A six-degree-of-freedom micro-vibration acoustic isolator for low-temperature radiation detectors based on superconducting transition-edge sensors, Rev. Sci. Instrum. **90**, 00 (2019).

[33] H. F. Hoevers, M. L. Ridder, A. Germeau, M. P. Bruijn, P. A. De Korte, and R. J. Wiegerink, Radiative ballistic phonon transport in silicon-nitride membranes at low temperatures, Appl. Phys. Lett. **86**, 1 (2005).

[34] See Supplemental Material at http://link.aps.org/supplemental/10.1103/PhysRevApplied.16.044059 for additional information on the $P(T_b)$, measured T_C for all devices, $I_C(B)$ curves for all geometries, and an example of (fits to) the measured complex impedance.

[35] M. A. Lindeman, S. Bandler, R. P. Brekosky, J. A. Chervenak, E. Figueroa-Feliciano, F. M. Finkbeiner, M. J. Li, and C. A. Kilbourne, Impedance measurements and modeling of a transition-edge-sensor calorimeter, Rev. Sci. Instrum. **75**, 1283 (2004).

[36] E. Taralli, P. Khosropanah, L. Gottardi, K. Nagayoshi, M. L. Ridder, M. P. Bruijn, and J. R. Gao, Complex impedance of TESs under AC bias using FDM readout system, AIP Adv. **9**, 045324 (2019).

[37] L. Gottardi, M. de Wit, E. Taralli, K. Nagayashi, and A. Kozorezov, Voltage Fluctuations in ac Biased Superconducting Transition-Edge Sensors, Phys. Rev. Lett. **126**, 217001 (2021).

[38] S. J. Smith, J. S. Adams, S. R. Bandler, G. Betancourt-Martinez, J. A. Chervenak, M. E. Eckart, F. M. Finkbeiner, R. L. Kelley, C. A. Kilbourne, S. J. Lee, F. S. Porter, J. E. Sadleir, and E. J. Wassell, Uniformity of kilo-pixel arrays of transition-edge sensors for X-ray astronomy, IEEE Trans. Appl. Supercond. **25**, 1 (2014).

[39] K. D. Irwin, An application of electrothermal feedback for high resolution cryogenic particle detection, Appl. Phys. Lett. **66**, 1998 (1995).

[40] A. Kozorezov, J. K. Wigmore, A. A. Golubov, D. D. Martin, P. A. De Korte, M. A. Lindeman, R. A. Hijmering, J. Van Der Kuur, H. F. Hoevers, L. Gottardi, and M. Y. Kupriyanov, Electrical noise in a TES as a resistively shunted conducting junction, J. Low. Temp. Phys. **167**, 108 (2012).

[41] A. Wessels, K. Morgan, J. D. Gard, G. C. Hilton, J. A. B. Mates, C. D. Reintsema, D. R. Schmidt, D. S. Swetz, J. N. Ullom, L. R. Vale, and D. A. Bennett, A model for excess johnson noise in superconducting transition-edge sensors, Appl. Phys. Lett. **118**, 202601 (2021).

[42] N. A. Wakeham, J. S. Adams, S. R. Bandler, S. Beaumont, J. A. Chervenak, A. M. Datesman, M. E. Eckart, F. M. Finkbeiner, R. Hummatov, R. L. Kelley, C. A. Kilbourne, A. R. Miniussi, F. S. Porter, J. E. Sadleir, K. Sakai, S. J. Smith, and E. J. Wassell, Thermal fluctuation noise in Mo/Au superconducting transition-edge sensor microcalorimeters, J. Appl. Phys. **125**, 164503 (2019).

[43] M. R. Palosaari, K. M. Kinnunen, I. J. Maasilta, M. Ridder, J. van der Kuur, and H. F. Hoevers, Analysis of impedance and noise data of an x-ray transition-edge sensor using complex thermal models, J. Low. Temp. Phys. **167**, 129 (2012).

[44] I. J. Maasilta, Complex impedance, responsivity and noise of transition-edge sensors: Analytical solutions for two- and three-block thermal models, AIP Adv. **2**, 00 (2012).

[45] M. Tinkham, *Introduction to Superconductivity* (McGraw-Hill, Inc., New York, 1996), 2nd ed.

[46] N. A. Wakeham, J. Adams, S. Bandler, S. Beaumont, M. Chang, J. Chervenak, M. Eckart, F. Finkbeiner, J. Ha, R. Hummatov, R. L. Kelley, C. A. Kilbourne, A. R. Miniussi, H. Muramatsu, F. S. Porter, J. E. Sadleir, K. Sakai, S. J. Smith, and E. J. Wassell, The impact of transition-edge sensor design on internal thermal fluctuation noise and thermal conductance, Poster Presentation ASC (2020).

[47] L. Gottardi, S. J. Smith, A. Kozorezov, H. Akamatsu, J. van der Kuur, S. R. Bandler, M. P. Bruijn, J. A. Chervenak, J. R. Gao, R. H. den Hartog, B. D. Jackson, P. Khosropanah, A. Miniussi, K. Nagayoshi, M. Ridder, J. Sadleir, K. Sakai, and N. Wakeham, Josephson effects in frequency-domain multiplexed TES microcalorimeters and bolometers, J. Low. Temp. Phys. **193**, 209 (2018).